RSC Advances

PAPER

View Article Online
View Journal | View Issue

Cite this: *RSC Adv.*, 2025, **15**, 32271

MEDT insights into the mechanism and selectivity of the (3 + 2) cycloaddition of (*Z*)-*N*-methyl-*C*-(2-furyl)-nitrone with but-2-ynedioic acid and the bioactivity of the reaction products

Mohamed Chellegui, [ab] Lakhdar Benhamed, [c] Raad Nasrullah Salih, [d] Ines Salhi,[b] Sofiane Benmetir, [ef] Ali Ben Ahmed, *[gh] Haydar A. Mohammad-Salim [ij] and Jesus Vicente de Julián-Ortize [e]

In this contribution, Molecular Electron Density Theory (MEDT) is employed to investigate the (3 + 2) cycloaddition reaction between (*Z*)-*N*-methyl-*C*-(2-furyl)-nitrone **1** and but-2-ynedioic acid **2**. DFT calculations at the M06-2X-D3/6-311+G(d,p) level of theory under solvent-free conditions at room temperature show that this reaction proceeds *via* **CA3-Z** diastereoselectivity, with the formation of the **CA3-Z** cycloadduct being both thermodynamically and kinetically more favoured than the **CA4-Z** one. Reactivity parameters obtained from CDFT calculations reveal that compound **1** predominantly behaves as a nucleophile with moderate electrophilic features, in contrast to compound **2**, which demonstrates strong electrophilicity and limited nucleophilic ability. This disparity in electronic properties suggests a polar mechanism for the investigated 32CA reaction. Then, bonding evolution theory shows that this cycloaddition proceeds *via* a one-step asynchronous process. On the other hand, both **CA3-Z** and **CA4-Z** cycloadducts demonstrate promising characteristics as lead compounds for drug development. Molecular docking studies indicate moderate affinity toward the 7BV2 protease, while their physicochemical properties and compliance with major drug-likeness rules support their potential as orally bioavailable agents. Furthermore, PASS predictions suggest a wide range of biological activities, notably in inflammation, neuroprotection, and anticancer applications. These findings, in line with experimental cytotoxicity data, highlight the therapeutic potential of these isoxazolidine derivatives and warrant further experimental validation.

Received 11th June 2025
Accepted 29th August 2025

DOI: 10.1039/d5ra04143k

rsc.li/rsc-advances

1. Introduction

The (3 + 2) cycloaddition (32CA) reactions are widely utilized synthetic strategies for constructing five-membered heterocycles.[1,2] Isoxazoline derivatives hold a distinctive position as key synthetic intermediates in the development of various natural products and biologically significant compounds. Notably, they exhibit diverse pharmacological properties, including anti-inflammatory, anti-cancer,[3] anti-malarial,[4] anti-tuberculosis,[5] and antithrombotic.[6] Density Functional Theory (DFT),[7] which relies on the foundational Hohenberg–Kohn principles,[8] and the Kohn–Sham approach,[9] has emerged as a powerful tool for predicting and understanding chemical behavior with high theoretical precision.

As a result, DFT has garnered significant attention from theoretical chemists over the past two decades. To address these challenges, Domingo introduced Molecular Electron Density Theory (MEDT),[10–12] which has significantly reshaped how reactivity is understood in the field of organic chemistry.[10–12] MEDT emphasizes that the primary determinant of reactivity is

[a]*Laboratory of Organic Chemistry (LR17ES08), Faculty of Sciences, University of Sfax, 3038 Sfax, Tunisia*
[b]*Namur Institute of Structured Matter, University of Namur, Rue de Bruxelles, 61, B-5000 Namur, Belgium*
[c]*Laboratory of Applied Thermodynamics and Molecular Modelling, Department of Chemistry, Faculty of Sciences, Abou-Bekr Belkaid University, P. O. 119, Tlemcen, 13000, Algeria*
[d]*Nursing Department, Bardarash Technical Institute, Akre University for Applied Science, Duhok 42001, Kurdistan Region, Iraq*
[e]*Process and Environmental Engineering Laboratory (LIPE), Faculty of Chemistry, University of Science and Technology of Oran Mohamed Boudiaf, P. O. Box 1503, El Mnaouer, 31000 Oran, Algeria*
[f]*Department of Physical Chemistry, Faculty of Pharmacy, University of Valencia, Av. Vicente Andrés Estellés s/n, 46100 Valencia, Spain*
[g]*University of Sfax, Faculty of Sciences of Sfax, Department of Physics, Laboratory of Applied Physics, Sfax, Tunisia. E-mail: ali.benahmed@isbs.usf.tn*
[h]*University of Sfax, Higher Institute of Biotechnology of Sfax, Department of Biomedical, Sfax, Tunisia*
[i]*Department of Chemistry, Faculty of Science, University of Zakho, Zakho 42002, Kurdistan Region, Iraq*
[j]*TCCG Lab, Scientific Research Center, University of Zakho, Zakho 42002, Kurdistan Region, Iraq*

the variation in electron density throughout a reaction. In the context of 32CA reactions, MEDT classifies these reactions into four distinct types: pseudodiradical (pdr),[13] pseudo(mono) radical (pmr),[14] carbenoid (cb),[13] and zwitterionic (zw),[15] which are respectively abbreviated as pdr-type, pmr-type, cb-type, and zw-type. Reaction type classification is determined by the electronic features of the three-atom components (TACs). A region with a single electron (1e) in a monosynaptic basin denotes a pseudoradical center, while two electrons (2e) correspond to a carbenoid site. TACs exhibiting two such pseudoradical centers are labeled pseudodiradicals; those with only one are termed pseudo(mono)radicals. If neither carbenoid nor pseudoradical centers are present, the TAC is classified as zwitterionic. These classifications define the pseudo(di)radical, pseudo(mono)radical, carbenoid, and zwitterionic characteristics of TACs. Furthermore, the relative reactivity order among these 32CA reaction types follows the trend: pdr > pmr > cb > zw. Pdr-type cycloaddition reactions progress rapidly *via* early transition states, whereas zw-type reactions require either nucleophilic or electrophilic activation to achieve satisfactory reaction rates.[16,17]

In addition, the MEDT framework integrates a variety of quantum chemical methods, including the Conceptual Density Functional Theory (CDFT).[18–20] This approach introduces key reactivity descriptors, such as the electronic chemical potential (μ),[18] electronegativity (χ), hardness (η),[21] softness (S), electrophilicity (ω),[22] and nucleophilicity (N).[23] The latter two have been particularly useful in explaining the polarity of 32CA reactions.

Molecular Fukui functions,[24,25] as formulated by Parr and Yang in the context of CDFT, provide a means to map global reactivity indices to specific atoms within a molecular structure. These local reactivity descriptors are crucial for identifying the most electrophilic and nucleophilic centers of a molecule, highlighting its local reactivity and shedding light on the regioselectivity of 32CA reactions. In parallel, complementary quantum mechanical theories have been developed to analyze molecular electron density. Among these are Bader's Quantum Theory of Atoms-in-Molecules (QTAIM)[26] and Becke and Edgecombe's Electron Localization Functions (ELFs),[27] which provide essential tools for understanding the distribution of electron density in molecules. Chemical bond characterization and its evolution along reaction coordinates have been effectively studied using ELFs and QTAIM methodologies. By combining the ELF functions with Thom's catastrophe,[28] Krokidis *et al.*[29,30] have defined Bonding Evolution Theory (BET) as a topological tool for the deciphering of bond breaking or forming signatures along a given chemical pathway. In the context of BET, a chemical reaction is viewed as a sequence of elementary chemical processes separated by catastrophes, which are seen as bond-forming or bond-breaking events. Since its inception, BET has demonstrated its robustness in tracking the chemical bond-forming or breaking process along the reaction pathway of many organic reactions.[31,32]

By leveraging these tools, MEDT has provided profound insights into various facets of 32CA reactions. Specifically, it has elucidated key aspects such as strain promotion,[33] regioselectivity,[34] chemoselectivity,[35] stereoselectivity,[36] and substituent effects.[37] These advances have refined our understanding of how molecules react and how complex organic mechanisms operate. According to MEDT, 32CA reactions should be categorized by polarity—either polar or non-polar—rather than as classic pericyclic reactions with synchronous or asynchronous pathways.[38–41] Both concerted and stepwise mechanisms, the latter involving acyclic intermediates, are possible under polar as well as nonpolar conditions. In the case of non-polar 32CA reactions, the resulting intermediate exhibits a biradical character.[42–45]

In 2019, Chakraborty introduced an innovative mechanochemical strategy for the synthesis of (*E*)-*N*-methyl-*C*-(2-furyl)-nitrone **1**, followed by 32CA reactions with activated alkenes and electron-deficient alkynes, using the ball milling technique. This solvent-free and environmentally friendly method proved to be remarkably efficient, significantly accelerating reaction rates and affording high yields of isoxazoline derivatives (Scheme 1). A comparative study with the corresponding solvent-free microwave-assisted reactions highlighted the superiority of ball milling. Notably, the cycloaddition between (*E*)-*N*-methyl-*C*-(2-furyl) nitrone **1** and but-2-ynedioic acid **2** resulted in the formation of 2-methyl-3-furyl-2,3-dihydroisoxazole-4,5-dicarboxylic acid **3** in an excellent yield of 91%. However, the stereochemistry of this isoxazoline derivative could not be determined in detail, as the key protons at the 4-H and 5-H positions were absent, and the single singlet signal corresponding to the 3-H proton was insufficient for stereochemical assignment.[46] Moreover, the newly synthesized compounds exhibited promising anticancer activity, underscoring the pharmaceutical potential of this synthetic approach.[42]

In this work, we present a comprehensive theoretical investigation of 32CA reaction between (*Z*)-*N*-methyl-*C*-(2-furyl)-nitrone **1** and but-2-ynedioic acid **2** within the MEDT framework (Scheme 2). Our primary goal is to deepen the understanding of the electronic, steric, and orbital factors governing the reactivity and stereoselectivity of this important class of cycloadditions, which remain fundamental in synthetic organic chemistry. Unlike many previous studies that focus mainly on general mechanistic aspects, we employ advanced methods such as BET to provide a detailed analysis of the sequence of bond formation and cleavage, revealing subtle mechanistic features that more precisely explain the reaction pathway. Furthermore, we investigate the origin of the **CA3-Z**/**CA4-Z** diastereoselectivity by elucidating the key electronic and steric factors that dictate the preferential formation of one

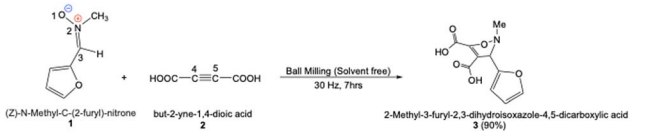

Scheme 1 32CA reaction of (*Z*)-*N*-methyl-*C*-(2-furyl)-nitrone **1** with but-2-ynedioic acid **2** for the synthesis of 2-methyl-3-furyl-2,3-dihydroisoxazole-4,5-dicarboxylic acid **3**.

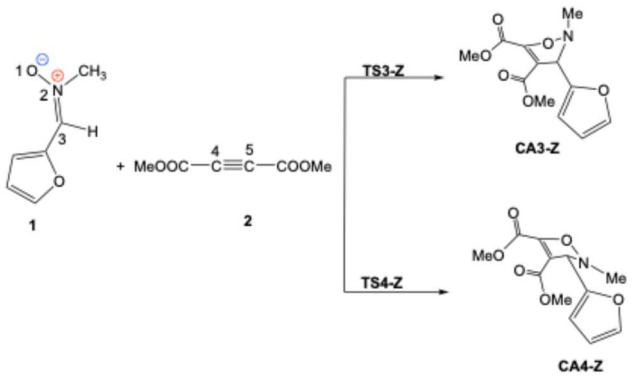

Scheme 2 Possible diastereoisomeric pathways for the 32CA reaction between (*Z*)-*N*-methyl-*C*-(2-furyl)-nitrone **1** and but-2-ynedioic acid **2**.

diastereomer over the other. In addition to the mechanistic insights, we integrate a bioinformatics perspective by evaluating the drug-likeness and biological potential of the resulting cycloadducts through molecular docking, ADMET (Absorption, Distribution, Metabolism, Excretion, and Toxicity) predictions, and PASS (Prediction of Activity Spectra for Substances) analysis. This multidimensional approach not only advances fundamental mechanistic knowledge but also explores the therapeutic relevance of these compounds, thus providing a strong foundation for the rational design of novel bioactive molecules with high therapeutic potential.

2. Computational methods

In the present contribution, density functional theory (DFT) calculations with the M06-2X exchange-correlation functional[43] and the 6-311+G(d,p) basis set is used to optimize the geometries of the equilibrium structures for all the stationary points involved in this 32CA reaction (reactants, products, and transition states (TSs)). The approach offers dependable estimates of thermodynamic and kinetic properties in organic processes,[44,45] with the D3 correction included to address dispersion forces.[46] Vibrational frequencies were calculated to validate the stationary character of the reactants and products (no imaginary frequency) as well as TSs (one imaginary frequency). The intrinsic reaction coordinate (IRC) path[47] was calculated, where the energy profiles validate that each transition state (TS) links the corresponding minima (reactants and the product). Calculations of all critical structures were performed at temperature $T = 298$ K and pressure $p = 1$ atm. All calculations were carried out with the Gaussian 16 software package.[48]

The polar character of the reaction is determined by calculating the global electron density transfer (GEDT),[49] which is obtained from the sum of the partial atomic charges (q) of the atoms corresponding to each framework (f) at the transition states (TSs), using the partial charge analysis from the Natural Bond Orbital (NBO) method.[50]

To perform Non-Covalent Interaction (NCI) analysis,[51] single-point energy calculations were carried out on each optimized transition state structure. Subsequently, plots of electron density [$\rho(r)$] against the reduced density gradient [$s(\mathbf{r}) = |\nabla\rho(\mathbf{r})|/2(3\pi^2)^{1/3}\rho(\mathbf{r})^{4/3}$] were generated using the NCIPLOT software.[52]

To assess the nature of the bonding characteristics of the forming and breaking bonds occurring along the reaction pathways, ELF and QTAIM analyses were initially performed using the Multiwfn program.[53] Subsequently, to elucidate the bond formation process along the reaction coordinate, a BET analysis was conducted by extracting the wavefunction at each point of the IRC paths. The ELF analysis was carried out using the TopMod package,[54] with a grid step of 0.2 bohr. Lastly, the positions and populations of the ELF basins were visualized with the DrawMol and DrawProfile programs.[55,56]

On the other hand, molecular docking studies of the isoxazoline compounds were conducted using Cresset Flare v9.69 to explore their potential biological activity.[57] To evaluate the primary antimicrobial properties of both compounds, predictions were made using the PASS online server.[58] The three-dimensional structures of the target proteins were obtained from the Protein Data Bank (PDB) (**https://www.rcsb.org**). Additionally, ADMET predictions were performed using both the SwissADME tool and the ADMETlab 3.0 web server.

3. Results and discussion

3.1 ELF and NPA characterizations of the reactants

As discussed in the Introduction section, the reactivity of TACs can be directly linked to their electronic structure.[59,60] Accordingly, a topological analysis of the ELF was first performed on nitrone **1** and but-2-ynedioic acid **2**. The ELF valence basin representations, attractor positions, electron populations, natural population analysis (NPA) charges, and derived Lewis structures for both reagents are presented in Fig. 1. In the case of nitrone **1**, the electron localization function identifies two monosynaptic basins associated with atom O1, namely V(O1) and V′(O1), totalling 5.86 electrons. Furthermore, one disynaptic basin between N2 and C3 (V(N2,C3)) holds 3.85*e*, and

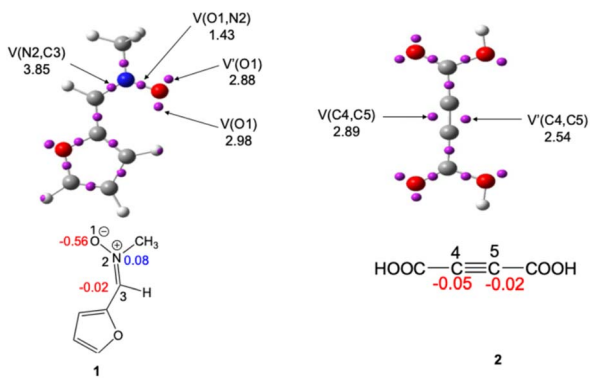

Fig. 1 Positions of ELF basin attractors for (*Z*)-*N*-methyl-*C*-(2-furyl)-nitrone **1** and but-2-ynedioic acid **2** calculated at 289.15 K. The figure also shows the proposed Lewis-like structures alongside the average natural atomic charges (in electrons, e).

another between O1 and N2 (V(O1,N2)) accounts for 1.43*e*. The two monosynaptic basins, V(O1) and V′(O1), are indicative of lone pair electrons on the O1 atom. The disynaptic basin V(O1,N2) is associated with the σ bond between O1 and N2, whereas the V(N2,C3) basin points to an electron-deficient π-bond between N2 and C3. On the other hand, ELF of **2** shows the presence of two V(C4,C5) and V′(C4,C5) disynaptic basins associated with the C4–C5 triple bonding region, integrating a total population of 5.43*e*.

The NPA findings for nitrone **1** show that O1 is significantly electron-rich with a charge of −0.56*e*, in contrast to N2 and C3, which exhibit only slight charge deviations at +0.08*e* and −0.02*e*. Taken together, the results support that charge separation is a significant factor influencing the electronic features characteristic of the TAC in (*Z*)-*N*-methyl-*C*-(2-furyl)-nitrone **1**. The analysis of the natural atomic charges reveals that both C4 and C5 carbon atoms in compound **2** carry negligible negative charges of −0.05 and −0.02*e*, respectively.

3.2 Analysis of the global and local reactivity indices

Several studies have shown that the reactivity indices derived from the CDFT approach is a very important tool in understanding the reactivity of molecules in organic reactions.[61–64] These indices including the energies of both the highest occupied molecular orbital (HOMO, ε_H) and the lowest unoccupied molecular orbital (LUMO, ε_L), the global electrophilicity ($\omega = \mu^2/2\eta$),[22] the chemical potential [$\mu = (\varepsilon_H + \varepsilon_L)/2$],[18] and the global hardness ($\eta = \varepsilon_L - \varepsilon_H$),[21] the nucleophilicity index (N)[23] ($N = \varepsilon_H$ (Nu) − ε_H (TCE) where Nu is the nucleophile and TCE is the tetracyano-ethylene reference, ε_H (TCE) = −10.9 eV at the M06-2X/D3/6-311+G(d,p)). The values of the CDFT reactivity indices at the ground state of the two reagents are given in Table 1.

The electronic chemical potential of (*Z*)-*N*-methyl-*C*-(2-furyl)-nitrone **1** ($\mu = -3.8$ eV) is very higher than that of but-2-ynedioic acid **2** ($\mu = -5.8$ eV), indicating that along this 32CA reaction, the flux of the electron density transfer will take place from **1** to **2**, and subsequently this reaction is classified as forward electron density flux (FEDF) reactions.[16,17,65]

According to Domingo's electrophilicity and nucleophilicity criteria,[66] compound **1** qualifies as a moderate electrophile with $\omega = 1.1$ eV and a strong nucleophile ($N = 3.93$ eV), while compound **2** is categorized as a strong electrophile ($\omega = 1.8$ eV) exhibiting low nucleophilicity ($N = 0.5$ eV) (refer to Table 1).

In polar reactions with asymmetric electrophile/nucleophile pairs, the most favorable mechanism often involves the initial contact between the electrophile's dominant electrophilic site and the nucleophile's principal nucleophilic site.[67] Among the various local reactivity indices developed within the framework of CDFT to characterize such localized behaviours, the nucleophilic and electrophilic Parr functions, introduced by Domingo in 2013,[68] have proven to be the most reliable tools for predicting and rationalizing local reactivity in both polar and ionic processes. These functions are based on changes in spin electron density resulting from the GEDT from the nucleophile to the electrophile.[69] Local reactivity descriptors were derived from the electron densities of the reactants as well as their radical anions and cations (Fig. 2), with the results compiled in Table S1. Analysis of the electrophilic P_k^+ Parr function for compound **2** shows that both C4 and C5 carbon atoms (see Scheme 2 for atom numbering) exhibit identical P_k^+ values of 0.20, suggesting that these two atoms are among the most electrophilic sites within the molecule. On the other hand, the nucleophilic P_k^- Parr function of **1** indicates that the oxygen atom O1 is the most nucleophilic center with a value, $P_k^- = 0.53$. Therefore, the interaction of the HOMO of the nitrone **1** and the LUMO of **2** leads first to the formation of the O1–C4 bond and then of the C3–C5 bond.

Table 1 Computed CDFT parameters (eV) of reactants

Reactants	ε_H	ε_L	μ	η	ω	N
1	−7.0	−0.6	−3.8	6.4	1.1	3.9
2	−10.5	−1.0	−5.8	9.5	1.8	0.5

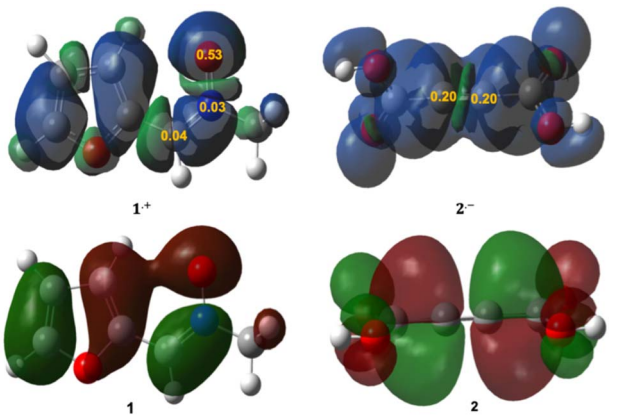

Fig. 2 Three-dimensional representations of the spin electron densities ($\eta = 0.02$) for the radical cation **1**$^+$ and radical anion **2**$^-$, alongside the nucleophilic Parr functions P_k^- for **1**, and electrophilic Parr functions P_k^+ for **2**, compared with the HOMO of **1** and the LUMO of **2**.

3.3 Analysis of the PES along the feasible stereoisomeric pathways

Due to the non-symmetry of the reagents, the 32CA reaction between (*Z*)-*N*-methyl-*C*-(2-furyl)-nitrone **1** and but-2-ynedioic acid **2** can occur through two diastereomeric reaction channels, namely **CA3-Z** and **CA4-Z** (Scheme 2). Thereby, in this 32CA reaction, two transition states, named **TS3-Z**, and **TS4-Z**, leading to the corresponding two possible cycloadducts, **CA3-Z**, and **CA4-Z**, respectively, which have been located and characterized (Scheme 2 and Table 2).

Table 2 indicates that the studied 32CA reaction exhibits a highly exothermic [ΔH(**CA3-Z**/**CA4-Z**) < 0] and exergonic [ΔG(**CA3-Z**/**CA4-Z**) < 0] characters. On the other hand, the formation of the **CA3-Z** cycloadduct is slightly more exothermic (Fig. 3) and exergonic (Fig. S1) than the **CA4-Z** product. This indicates that the **CA3-Z** product is slightly more thermodynamically favoured than the **CA4-Z** one. The **CA3-Z** pathway

Table 2 Thermodynamic parameters for the stationary points involved in the studied 32CA reaction, *in vacuo*

	ΔE (kcal mol^{-1})	ΔH (kcal mol^{-1})	ΔS (cal mol^{-1} K^{-1})	ΔG (kcal mol^{-1})
CA3-Z	−50.8	−48.5	−49.6	−33.7
CA4-Z	−50.5	−48.3	49.2	−33.5
TS3-Z	6.0	6.4	−44.5	19.6
TS4-Z	6.9	7.5	−44.7	20.9

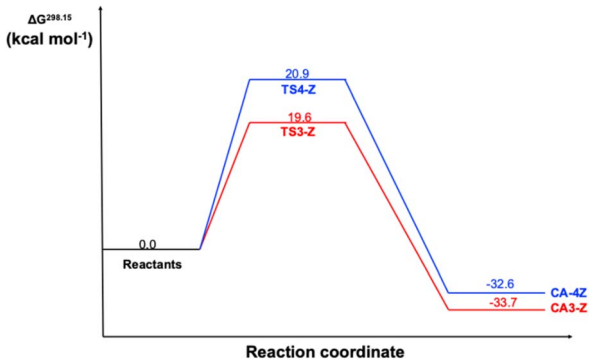

Fig. 3 Relative Gibbs free energy diagram of the 32CA reaction between (*Z*)-*N*-methyl-*C*-(2-furyl)-nitrone **1** and but-2-ynedioic acid **2**, at the M06-2X/D3/6-311+G(d,p) level of approximation, *in vacuo*.

exhibits the low activation energy compared to the **CA4-Z** one [ΔX(**TS3-Z**) < ΔX(**TS4-Z**), with $X = E$, $H°$ and $G°$], with a very low difference of activation Gibbs free energy between the two pathways is observed [ΔG(**TS4-Z**) − ΔX(**TS3-Z**) = 1.3 kcal mol^{-1}] (Fig. 3). From this analysis, it can be noticed that the **CA3-Z** pathway is also kinetically slightly more favoured than the **CA4-Z** one. On the other hand, the calculated value of the Boltzmann population,[70] which is about 78.9% and 21.1% for **CA3-Z** and **CA4-Z**, respectively. Therefore, these DFT calculations clearly indicate that the studied 32CA reaction proceeds with an **CA3-Z** stereochemistry, identifying **CA3-Z** as the major product and **CA4-Z** as the minor one. On the other hand, DFT calculations performed at the same level of theory reveal that the inclusion of a nonpolar solvent, such as cyclohexane, does not significantly affect the predictions obtained in the gas phase for the 32CA reaction between (*Z*)-*N*-methyl-*C*-(2-furyl)-nitrone **1** and but-2-ynedioic acid **2**. A slight increase of less than 2 kcal mol^{-1} in the reaction and activation energies is observed (Table S3). On the other hand, DFT results show that the diastereoselectivity of the 32CA reaction between (*Z*)-*N*-methyl-*C*-(2-furyl) nitrone **1** and dimethyl but-2-ynedioate **2** (Scheme S2) closely resembles that observed with but-2-ynedioic acid **2**, indicating that the ester substitution does not significantly alter the preferred diastereomer formation (Table S5).

The geometries of the TSs involved in the 32CA reaction between and, and for both **CA3-Z** and **CA4-Z** pathways are depicted in the Fig. 4, together with the O1–C4 and C3–C5 bond lengths (nomenclature is shown in Scheme 2). For **TS3-Z**, the lengths of the O1–C4 and C3–C5 forming bonds are 1.81 Å and 2.40 Å, respectively. For **TS4-Z**, the lengths of the O1–C4 and C3–C5 forming bonds are 1.87 Å and 2.33 Å, respectively.

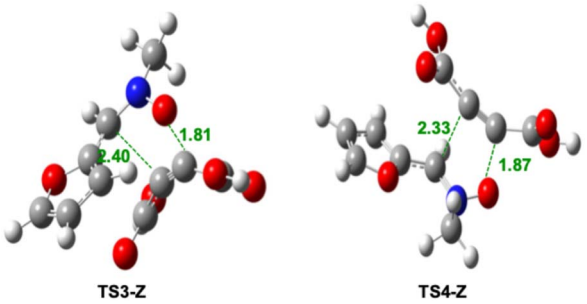

Fig. 4 Geometries of the TSs of the 32CA reaction between **1** and **2**, *in vacuo*. The C3–C5 and O1–C4 distances values are given in Å.

An in-depth evaluation of the stationary points was performed to determine the degree of asynchronicity in the transition states. The relevant metrics, such as interatomic reactive center distances (r), distance progress index (l), and asynchronicity parameter (Δl),[71] are listed in Table 3. The values of distance progress indexes of the forming O1–C4 bond are 0.65, and 0.59, for **TS3-Z** and **TS4-Z**, respectively. While the C3–C5 bond show progress indexes of 0.41 and 0.46 in **TS3-Z**, and **TS4-Z**, respectively. These values indicate that, the formation of the O1–C4 bond is more advanced than that of the C3–C5 bond in both **TS3-Z** and **TS4-Z** pathways. This in good agreement with the analysis of the Parr functions (Section 3.2), which indicates that the first favourable interaction is between the O1 oxygen atom of nitrone **1** and the C4 carbon atom of **2**. On the other hand, the Δl values are 0.24 and 0.13, for **TS3-Z** and **TS4-Z**, respectively. These findings show that the 32CA reaction follows a one-step asynchronous pathway, where **TS3-Z** is marginally more asynchronous than **TS4-Z**. The vibrational mode corresponding to the singular imaginary frequency (353i in **TS3-Z** and 318i in **TS4-Z**) primarily involves the displacement of O1, C3, C4, and C5 atoms along the forming C3–C5 and O1–C4 bonds. Assessing the reaction's polarity involved calculating the GEDT as the aggregate of natural atomic charges from the but-2-ynedioic acid **2** moiety. The GEDT values are 0.21 and 0.17e for **TS3-Z** and **TS4-Z**, respectively, highlighting the polar character of this 32CA reaction. According to Domingo's polar/non-polar classification,[72] reactions with GEDT values close to 0.0e are

Table 3 Key parameters of the critical structure parameters of the 32CA reaction between (*Z*)-*N*-methyl-*C*-(2-furyl)-nitrone **1** and but-2-ynedioic acid **2**[a]

	r_{C3-C5} (Å)	l_{C3-C5}	r_{O1-C4} (Å)	l_{O-C}	Δl
TS3-Z	2.40	0.41	1.81	0.65	0.24
CA3-Z	1.51		1.34		
TS4-Z	2.33	0.46	1.87	0.59	0.13
CA4-Z	1.52		1.34		

[a] $l_{C-C} = 1 - \frac{r^{TS}_{C3-C5} - r^{P}_{C3-C5}}{r^{P}_{C3-C5}}$; $l_{O-C} = 1 - \frac{r^{TS}_{O1-C4} - r^{P}_{O1-C4}}{r^{P}_{O1-C4}}$; $\Delta l = |l_{C3-C5} - l_{O1-C4}|$.

considered non-polar, whereas those with values exceeding 0.2*e* are indicative of polar processes. The positive GEDT values indicates that the electron density transfer will takes place from the nitrone **1** framework toward the but-2-ynedioic acid **2** one, supporting a FEDF nature of this reaction,[65] which is in good agreement with the CDFT analysis (Section 3.2).

3.4 ELF topological analysis of the TSs

An ELF study of the transition states was performed to elucidate their electronic features. The major valence basin populations and basin attractor coordinates for **TS3-Z** and **TS4-Z** can be found in Fig. 5. The two TSs show the presence of a V(N2) monosynaptic basin, integrating a total population of 1.26 and 1.15*e*, at **TS3-Z** and **TS4-Z**, respectively, associated with the non-bonding electron density created at the N2 nitrogen, which is absent in nitrone **1** (Fig. 1 and Section 3.1). The population of this monosynaptic basin arise from the V(N2,C3) disynaptic basin. Note that the N2–C3 bonding region, which integrates a total population of 3.85*e* at nitrone **1**, is depopulated to 2.77*e*, and 2.86*e*, at **TS3-Z**, and **TS4-Z**, respectively, suggesting the rupture of N2–C3 double bond. The TSs show also the presence of two monosynaptic basins, V(O1) and V′(O1), integrating a total population of 5.74*e* (**TS3-Z**) and 5.67*e* (**TS4-Z**), associated with the non-bonding electron density at the O1 oxygen. The V(O1,N2) disynaptic basin associated with the O1–N2 single bond shows a decrease in population from 1.43*e* at nitrone **1** to 1.23*e* and 1.26*e* at **TS3-Z** and **TS4-Z**, respectively. On the other hand, the V(C4,C5) and V′(C4,C5) disynaptic basins are depopulated from 5.43*e* at **2** to 4.63*e* and 4.82*e*, at **TS3-Z** and **TS4-Z**, respectively, suggesting the rupture of C4–C5 triple bond. This depopulation leads to the appearance of two pseudoradical centers at the C4 and C5 carbon atoms at both TSs, V(C4) and V(C5), integrating a total population of 0.11 and 0.66*e*, respectively.

3.5 AIM analysis

To gain deeper insight into the atomic interactions at the **TS3-Z** and **TS4-Z** of the 32CA reaction between (*Z*)-*N*-methyl-*C*-(2-furyl)-nitrone **1** and but-2-ynedioic acid **2**, a QTAIM topological analysis of the electron density (ρ) was performed. This analysis focused on the critical points (CPs) associated with the formation of the new C3–C5 and O1–C4 single bonds at the TSs (Fig. 6). The QTAIM parameters obtained are listed in Table 4.

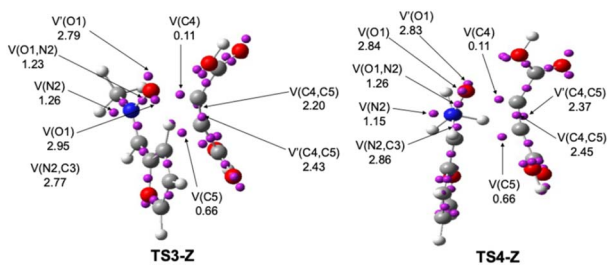

Fig. 5 M06-2X-D3/6-311+G(d,p) ELF localization domains ($\eta = 0.80$) and the positions of TSs attractor basins.

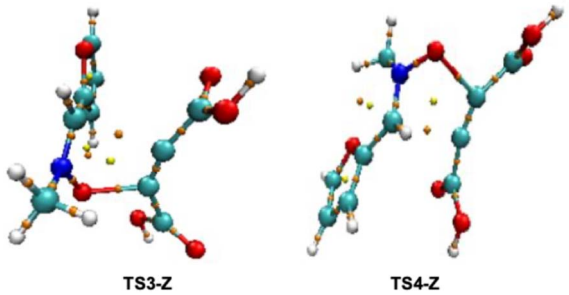

Fig. 6 AIM representation of the TSs involved in the studied 32CA reaction.

Both transition states show that the new critical points CP1 and CP2 have electron densities $\rho(r)$ under 0.1 a.u. The positive but low $\nabla^2\rho(r)$ value indicates that covalent bonding is not occurring in these interaction regions. Thus, the formation of the new C3–C5 and O1–C4 covalent bonds has not yet begun at the TS, which is in full agreement with the ELF analysis (absence of the new disynaptic basins V(C3,C5) and V(O1,C4), see Fig. 5), the geometrical structures (Fig. 4 and Section 3.3), and the BET analysis of the **TS3-Z** (Section 3.7), all of which confirm that the two new single bonds begin to form only after the transition state.

3.6 NCI analysis

The NCI analysis of the **TS3-Z** and **TS4-Z** structures associated with the 32CA reaction between (*Z*)-*N*-methyl-*C*-(2-furyl)-nitrone **1** and but-2-ynedioic acid **2** reveals significant differences in the nature and distribution of non-covalent interactions (Fig. 7). In **TS3-Z**, the presence of strong attractive interactions is evidenced by pronounced blue isosurfaces and a concentrated region in the attractive domain ($\mathrm{sign}(\lambda_2)\rho < 0$) of the NCI scatter plot. These interactions include well-defined intermolecular hydrogen bonds between the acidic protons of the carboxylic groups and electronegative centers (O or N) on the nitrone and the furan ring. Additionally, dipole–dipole interactions, stemming from the high polarity of both the nitrone and the electron-deficient alkyne diacid, further contribute to the stabilization of the transition state. Weak but favorable π–π stacking interactions between the furan moiety and the π-system of the alkyne may also be involved, as suggested by greenish blue isosurfaces. A substantial contribution from dispersion (van der Waals) interactions is also apparent, as indicated by extensive green isosurfaces and a dense central green region in the scatter plot. Conversely, **TS4-Z** exhibits

Table 4 Critical point electron density and Laplacian parameters for TSs

	CP1(O1–C4)		CP2(C3–C5)	
Structure	ρ	$\nabla^2\rho$	ρ	$\nabla^2\rho$
TS3-Z	0.055	0.112	0.042	0.053
TS4-Z	0.096	0.132	0.046	0.055

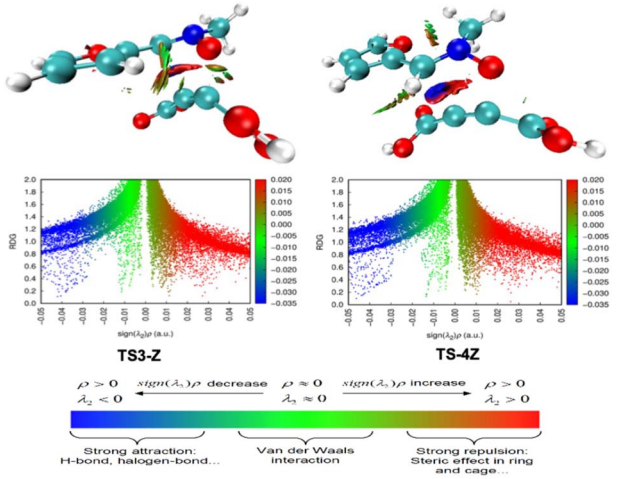

Fig. 7 NCI gradient isosurfaces ($\eta = 0.08$) and the reduced density gradient of the optimized TSs (**TS3-Z** and **TS4-Z**) associated with the 32CA reaction between (*Z*)-*N*-methyl-*C*-(2-furyl)-nitrone **1** and but-2-ynedioic acid **2**.

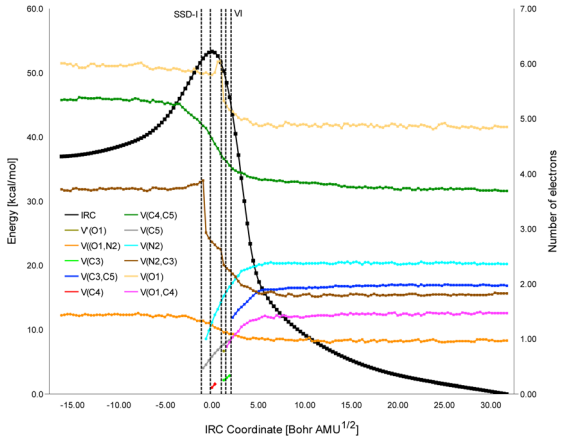

Fig. 8 Evolution of electron populations (in e) for selected ELF basins along the intrinsic reaction coordinate (IRC) corresponding to the **TS3-Z** pathway of the 32CA reaction between compounds **1** and **2**. The changes are illustrated atop the associated potential energy surface.

a markedly less favourable non-covalent interaction profile. Although some attractive interactions (*e.g.*, hydrogen bonding and dipole–dipole contacts) are still present, they appear geometrically suboptimal and less intense. The contribution from dispersion interactions is reduced, as shown by more diffuse green regions. Most notably, steric repulsions between bulky substituents such as the methyl group of the nitrone, the furan ring, and the carboxylic groups give rise to extensive red isosurfaces and a broadened distribution in the repulsive region ($\text{sign}(\lambda_2)\rho > 0$) of the scatter plot. These observations account for the enhanced stabilization of **TS3-Z** relative to **TS4-Z**, and thus for the observed stereoselectivity, which arises from a more favorable balance of attractive non-covalent interactions and minimized steric hindrance.

3.7 Bonding evolution theory (BET) analysis of the most favourable pathway: TS3-Z

In order to characterize the O1–C4 and C3–C5 bonds formation along the 32CA reaction between (*Z*)-*N*-methyl-*C*-(2-furyl)-nitrone **1** with but-2-ynedioic acid **2**, and thus to characterize the type of 32CA reaction, a BET study along the most favourable **TS3-Z** reaction path was performed. The electron population changes along the reaction pathway for the **TS3-Z** and the formation of **CA3-Z** are depicted in Fig. 8. According to the BET analysis, the formation of the new bonds (O3–C4 and C3–C4) occurs through six structural stability domains (SSDs). The first **SSD-I** domain describes the different topologies of the two reagents. Four basins are highlighted: the V(N2,C3) (3.72*e*), V(O1,N2) (1.43*e*), disynaptic basins and the V(O1) (6.01*e*, lone pairs) monosynaptic basin of **1** as well as the V(C4,C5) (5.34*e*) disynaptic basin of **2** (Fig. 9). At the **SSD-II**, two monosynaptic basins are created, V(C5) and V(N2), with 0.47 and 1.0*e*, respectively (fold-type catastrophe, *F*) (Fig. 8). They stem from the simultaneous reduction of the V(N2,C3) and V(C4,C5) disynaptic basin populations (Fig. 8). In the following domain (**SSD-III**), the population of the V(C4,C5) basin continuous decreases by 0.70*e*, leading to the formation of another new monosynaptic basin, V(C4), with 0.18*e*, *via* another *F* catastrophe. In **SSD-VI**, a fourth monosynaptic basin, V′(O1), with an electron population of 0.87*e*, appears on the oxygen atom due to the gradual depletion of the original V(O1) basin. At the same time, another *F* catastrophe also appears in this domain leading to the formation of a pseudoradical center on the C3 atom, V(C3), with a population of 0.25*e*. This increase results from the continuous loss of electron density in the V(N2,C3) basins, which undergo a depletion of 0.29*e*. The initial topological transition, observed in the **SSD-V** domain, involves the formation of the V(O1,C4) basin, associated with the O1–C4 bond *via* a cusp-C catastrophe. As **SSD-VI** begins, this new basin contains 0.86*e*, mainly sourced from the disappearing V(C4) basin and a 0.10*e* reduction from the V(O1) basin. Finally, the formation of a second C3–C5 single bond begins in **SSD-VI**, marking the final topological change. This occurs through the emergence of a new

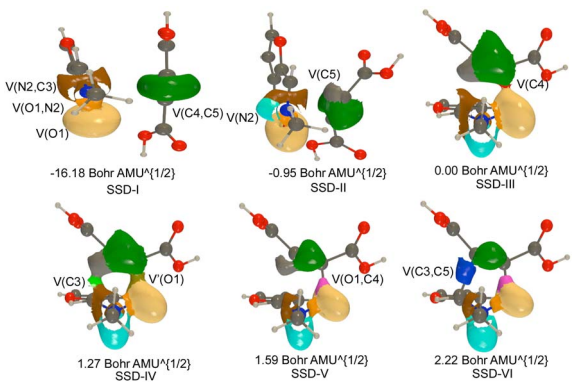

Fig. 9 ELF basin isosurfaces ($\eta = 0.75$) corresponding to representative points along the successive SSDs and associated Lewis structures along the IRC for the **TS3-Z** pathway of the 32CA reaction between **1** and **2**. Basin colors follow the labeling scheme shown in Fig. 8, and the intrinsic reaction coordinate value is indicated for each point.

disynaptic basin, V(C3,C5), resulting from the fusion of the previously formed monosynaptic basins V(C3) and V(C5). The population of this new basin increases from 1.39*e* to 1.97*e* throughout the domain.

3.8 Molecular docking against 7BV2

A molecular docking study was carried out to evaluate the binding interactions of the **CA3-Z** and **CA4-Z** cycloadducts with the SARS-CoV-2 main protease (PDB ID: 7BV2). The goal was to gain insight into their potential biological activity through structural analysis of their binding modes. Both isomers exhibited moderate binding affinities of −5.8 kcal mol^{-1} for **CA3-Z** and −5.2 kcal mol^{-1} for **CA4-Z**, whereas the native co-crystallized ligand showed a significantly stronger interaction at −12.4 kcal mol^{-1} (Table 5). These results suggest that the synthesized compounds can interact with the protease, albeit less effectively than the reference inhibitor. The 2D interaction diagrams reveal distinct binding profiles for **CA3-Z** and **CA4-Z** products within the 7BV2 active site (Fig. 10). **CA3-Z** forms hydrogen bonds with TYR A619 and the F86–P101 fragment, along with water-bridged interactions (HOH A1102, HOH A1104, HOH A1105), and is further stabilized by hydrophobic contacts, π–alkyl interactions (4MG A100, 5MG A100), and π–π stacking with TYR A619. In contrast, **CA4-Z** interacts *via* hydrogen bonds with ASP A618, TYR A619, and water molecules, and engages in similar hydrophobic and π–alkyl contacts, including a π–π or π–σ interaction with TRP A617. These interaction patterns illustrate the unique binding modes of each isomer and highlight their potential as lead structures for 7BV2 protease inhibition.

3.9 Drug-likeness assessment and ADMET predictions

Table 6 presents the drug-likeness predictions for the **CA3-Z** and **CA4-Z** compounds, as calculated using the SwissADME tool. Both compounds have an identical molecular weight of 239.04 daltons, which is well within the acceptable range for drug-like molecules. Each compound contains three rotatable bonds, indicating moderate molecular flexibility. They also have seven hydrogen bond acceptors and two hydrogen bond donors, which comply with the thresholds set by Lipinski's rule of five.

The topological polar surface area (TPSA) for both compounds is 100.21 Å^2, suggesting good potential for membrane permeability. Their lipophilicity, represented by a log *P* value of 0.436, falls within the optimal range for oral bioavailability. Importantly, neither compound has any Lipinski's rule violations, indicating strong potential as orally active drug candidates. Fig. 11 displays a physico-chemical

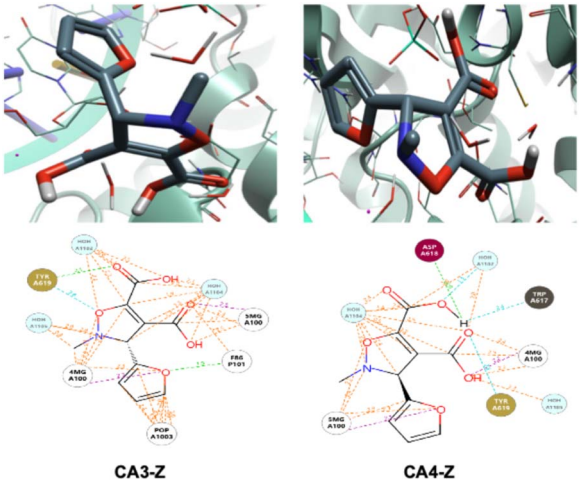

Fig. 10 Three-dimensional (3D) and two-dimensional (2D) interactions of CA3-Z and CA4-Z compounds with the 7BV2 protein.

radar chart comparing the properties of the selected lead **CA3-Z** and **CA4-Z** compounds. Each radar plot illustrates multiple molecular descriptors in a single graphical representation, allowing visual comparison of the compounds' drug-likeness profiles. The chart typically includes parameters such as size, polarity, solubility, lipophilicity, flexibility, and saturation.

Both **CA3-Z** and **CA4-Z** appear to share similar physicochemical characteristics, reflecting their comparable molecular structures and computed values. The balanced and centralized shape of the radar plots suggests that both compounds fall within the optimal range for oral bioavailability and drug development potential. The Lipinski,[73] Ghose,[74] Veber,[75] Egan,[76] and Muegge[77] rules are criteria used in drug design to predict whether a compound has oral bioavailability. These rules use several molecular descriptors, such as molecular weight (MW), logarithm of the partition coefficient (MLOGP, WLOGP, XLOGP3), number of donor and acceptor hydrogen bonds, topological polar surface area (TPSA), number of rotatable bonds, among others. The rules define acceptable ranges for these descriptors for a molecule to be, potentially, an oral drug.[78,79] Both **CA3-Z** and **CA4-Z** compounds are stereoisomers, which differ in the chirality of only one atom. Stereoisomers share the same druglike features. In this case, the values of the descriptors for **CA3-Z** and **CA4-Z** fall within the intervals of probable oral bioavailability for all the criteria studied (Table S6).

3.10 Assessment of antimicrobial activities based on PASS for the studied compounds

Finally, the biological activity spectra of the molecules were predicted using the PASS software, which estimates potential

Table 5 Docking affinity of the CA3-Z and CA4-Z compounds as well as the co crystal ligands for 7BV2, given in kcal mol^{-1}

Ligands	Affinity
CA3-Z	−5.8
CA4-Z	−5.2
Co-crystal	−12.4

Table 6 SwissADME-computed drug-likeness predictions for CA3-Z and CA4-Z compounds

MW	NROT	NHA	NHD	TPSA	log *P*	Lipinski's violations
239.04	3	7	2	100.21	0.436	0

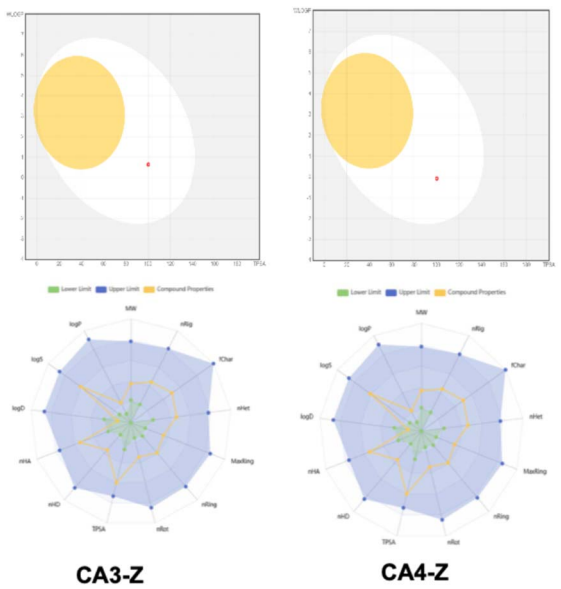

Fig. 11 Physico-chemical radar chart of the selected lead compounds in the dataset.

biological activities based on molecular structure. The results are presented as two probabilities: P_a (probability of activity) and P_i (probability of inactivity). Table 7 lists the predicted activities with the highest probability values for both **CA3-Z** and **CA4-Z** compounds. PASS analysis revealed that both **CA3-Z** and **CA4-Z** isoxazolidine derivatives show potential as anaphylatoxin receptor antagonists, which are either in use or under development for the treatment of inflammatory, autoimmune, neurodegenerative, and kidney diseases, as well as severe cases of COVID-19.[80]

In addition, these compounds demonstrated AMPA receptor agonist activity, suggesting possible applications in cognitive enhancement and neuropsychiatric disorders,[69,70] though such uses remain largely at the research stage. The predicted antiischemic and cerebral protective activities also support their relevance in the management of acute stroke and cerebrovascular diseases. Furthermore, PASS predicted that these compounds act as ubiquinol-cytochrome-c reductase inhibitors, targeting complex III of the mitochondrial electron transport chain. This activity is of particular interest due to its implication in antimicrobial treatments,[71] and cancer therapy, where mitochondrial dysfunction can trigger apoptosis in tumor cells.[81] These predicted activities align well with previously published cytotoxicity assays, in which isoxazolidine derivatives have garnered considerable attention as potential antineoplastic agents.[42,82–84]

Table 7 PASS prediction results for CA3-Z and CA4-Z cycloadducts showing activities with $P_a > 0.7$

Biological activity	P_a	P_i
Anaphylatoxin receptor antagonist	0.864	0.006
AMPA receptor agonist	0.807	0.001
Antiischemic, cerebral	0.805	0.014
Ubiquinol-cytochrome-c reductase inhibitor	0.745	0.052

4. Conclusions

In this work, Molecular Electron Density Theory (MEDT) is used to study the 32CA reaction between (*Z*)-*N*-methyl-*C*-(2-furyl)-nitrone **1** and but-2-ynedioic acid **2**. Global indices from the CDFT approach indicate that compound **1** is a moderate electrophile and strong nucleophile (ω = 1.13 eV; N = 3.93 eV), while compound **2** behaves as a strong electrophile with limited nucleophilic capacity (ω = 1.75 eV; N = 0.45 eV), following established classification criteria. The CDFT analysis also indicates that this 32CA reaction is classified as a forward electron density flux (FEDF) reaction, in which the global electron density transfer (GEDT) occurs from the dipole **1** to the dipolarophile **2**. Thermodynamic analysis reveals that the reaction proceeds with a clear preference for **CA3-Z** stereoselectivity, as the formation of the **CA3-Z** cycloadduct is both kinetically and thermodynamically more favourable than that of the **CA4-Z** isomer. DFT results confirm that solvent (cyclohexane) effects have a minimal impact on the reaction energetics and do not alter the gas-phase predictions for the 32CA reaction between (*Z*)-*N*-methyl-*C*-(2-furyl) nitrone **1** and but-2-ynedioic acid **2**. Moreover, the nature of the dipolarophile (acid *vs.* ester) does not significantly affect the observed diastereoselectivity. BET-based evaluation of the ELF profiles and TS geometries confirms that the process advances through an asynchronous single-step mechanism, with **CA3-Z** presenting a higher level of asynchronicity than **CA4-Z**. This asynchronicity is further supported by the analysis of Quantum Theory of Atoms in Molecules (QTAIM) descriptors. In both cases, the formation of the O1–C4 bond is more advanced than that of the C3–C5 bond at the transition state. These findings are in good agreement with the Parr function analysis, which identifies the O1 atom of nitrone **1** and the C4 atom of dipolarophile **2** as the most reactive centers, suggesting that the initial interaction takes place between them. On the other hand, the computed GEDT values at the TSs indicate that this 32CA reaction exhibits a polar character (GEDT $\approx$ 0.20*e*).

The study of biological activities of the **CA3-Z** and **CA4-Z** cycloadducts highlights promising characteristics as lead candidates for drug development. Molecular docking studies reveal moderate binding affinities toward the SARS-CoV-2 main protease (7BV2), with binding energies of −6.79 kcal mol^{-1} for **CA3-Z** and −6.81 kcal mol^{-1} for **CA4-Z**, which, although lower than that of the co-crystal ligand (−12.41 kcal mol^{-1}), suggest strong potential for further optimization. Physicochemical analysis confirms their drug-like properties, with a molecular weight of 239.04 Da, log *P* of 0.436, TPSA of 100.21 Å^2, and compliance with Lipinski's rule of five, as well as additional filters (Ghose, Veber, Egan, Muegge), indicating good oral bioavailability. Moreover, PASS predictions highlight a broad range of potential biological activities, including anaphylatoxin receptor antagonism, AMPA receptor agonism, and mitochondrial complex III inhibition. These findings align well with existing experimental data, particularly in the context of

inflammation, neuroprotection, and cancer therapy. Together, these results underscore the therapeutic potential of these isoxazolidine derivatives and warrant further experimental validation to explore their biological efficacy and clinical applicability.

Author contributions

Mohamed Chellegui, Ines Salhi, Sofiane Benmetir, Lakhdar Benhamed, and Raad Nasrullah Salih: writing, investigation, validation, methodology; Ali Ben Ahmed, Haydar A. Mohammad-Salim, and Jesus Vicente de Julián-Ortiz: validation, editing, reviewing, and supervision. All authors have read and approved the published version of the manuscript.

Conflicts of interest

There are no conflicts to declare.

Data availability

The data supporting this article have been included as part of the SI.

Supplementary information: Table with the M06-2X-D3/6-311+G(d,p) electronic energies, enthalpies, entropies and Gibbs free energies for the stationary points involved in the studied 32CA reaction. Table with local reactivity descriptors of the two reagents. Table with the result of five druglikeness rules evaluated for **CA3-Z** and **CA4-Z** compounds. Cartesian coordinates of the stationary points involved in this 32CA reaction calculated at the M06-2X-D3/6-311+G(d,p) level of theory, *in vacuo*. See DOI: **https://doi.org/10.1039/d5ra04143k**.

Acknowledgements

M. C. gratefully acknowledges the University of Namur (UNamur) for granting him the status of Scientific Collaborator, as well as the F.R.S. - FNRS for financially supporting his research stay at UNamur. J. V. de J.-O. is thankful for the financial support received from the Universitat de València through its Special Actions Program (ComPPETE, Ref. UV-INV-AE-3677056). The computational work was carried out using the resources of the Consortium des Équipements de Calcul Intensif (CÉCI, **https://www.ceci-hpc.be**), including those of the UNamur Technological Platform of High-Performance Computing (PTCI, **https://www.ptci.unamur.be**).

References

1 W. H. P. Albert Padwa, *Synthetic Applications of 1,3-Dipolar Cycloaddition Chemistry toward Heterocycles and Natural Products*, Wiley, 2002, vol. 59.
2 D. Rane and M. Sibi, Recent Advances in Nitrile Oxide Cycloadditions. Synthesis of Isoxazolines, *Curr. Org. Synth.*, 2011, **8**, 616–627.
3 G. Kumar and R. Shankar, 2-Isoxazolines: A Synthetic and Medicinal Overview, *ChemMedChem*, 2021, **16**, 430–447.
4 K. S. Vinay Kumar, G. S. Lingaraju, Y. K. Bommegowda, A. C. Vinayaka, P. Bhat, C. S. Pradeepa Kumara, K. S. Rangappa, D. C. Gowda and M. P. Sadashiva, Synthesis, antimalarial activity, and target binding of dibenzazepine-tethered isoxazolines, *RSC Adv.*, 2015, **5**, 90408–90421.
5 R. P. Tangallapally, D. Sun, B. Rakesh, N. Budha, R. E. B. Lee, A. J. M. Lenaerts, B. Meibohm and R. E. Lee, Discovery of novel isoxazolines as anti-tuberculosis agents, *Bioorg. Med. Chem. Lett.*, 2007, **17**, 6638–6642.
6 S. K. Prajapti, S. Shrivastava, U. Bihade, A. K. Gupta, V. G. M. Naidu, U. C. Banerjee and B. N. Babu, Synthesis and biological evaluation of novel Δ 2 -isoxazoline fused cyclopentane derivatives as potential antimicrobial and anticancer agents, *Medchemcomm*, 2015, **6**, 839–845.
7 J. Calais, Density-functional theory of atoms and molecules. R.G. Parr and W. Yang, Oxford University Press, New York, Oxford, 1989. IX + 333 pp. Price £45.00, *Int. J. Quantum Chem.*, 1993, **47**, 101.
8 P. Hohenberg and W. Kohn, Inhomogeneous Electron Gas, *Phys. Rev.*, 1964, **136**, B864–B871.
9 W. Kohn and L. J. Sham, Self-Consistent Equations Including Exchange and Correlation Effects, *Phys. Rev.*, 1965, **140**, A1133–A1138.
10 Z. Xiao, T. Ding, S. Mao, X. Ning and Y. Kang, ChemInform Abstract: Zinc Iodide-Mediated Direct Synthesis of 2,3-Dihydroisoxazoles from Alkynes and Nitrones, *ChemInform*, 2016, **47**(41), 1.
11 M. Ríos-Gutiérrez and L. R. Domingo, Unravelling the Mysteries of the [3+2] Cycloaddition Reactions, *Eur. J. Org. Chem.*, 2019, **2019**, 267–282.
12 H. Mohammad-Salim, R. Hassan, H. H. Abdallah and M. Oftadeh, Theoretical Study on the Mechanism of [3+2] Cycloaddition Reactions between α,β-unsaturated Selenoaldehyde with Nitrone and with Nitrile Oxide, *J. Mex. Chem. Soc.*, 2020, **64**(2), 74–91.
13 M. Ríos-Gutiérrez and L. R. Domingo, The carbenoid-type reactivity of simplest nitrile imine from a molecular electron density theory perspective, *Tetrahedron*, 2019, **75**, 1961–1967.
14 L. R. Domingo and M. Ríos-Gutiérrez, A Molecular Electron Density Theory Study of the Reactivity of Azomethine Imine in [3+2] Cycloaddition Reactions, *Molecules*, 2017, **22**, 750.
15 L. R. Domingo, M. Ríos-Gutiérrez and P. Pérez, A Molecular Electron Density Theory Study of the Reactivity and Selectivities in [3 + 2] Cycloaddition Reactions of C , N -Dialkyl Nitrones with Ethylene Derivatives, *J. Org. Chem.*, 2018, **83**, 2182–2197.
16 S. Benmetir, M. Chellegui, R. N. Salih, L. Benhamed, I. Salhi, H. A. Mohammad-Salim and J. V. de Julián-Ortiz, Decoding the [3 + 2] cycloaddition of a furan–imine oxide with styrene: mechanism, selectivity and bioactivity, *Org. Biomol. Chem.*, 2025, **23**, 6785–6800.
17 S. Benmetir, M. Chellegui, L. Benhamed, R. Mowafak Al-Mokhtar, R. N. Salih, M. A. Algso, J. V. de Julián-Ortiz and H. A. Mohammad-Salim, Mechanistic insights into the regio- and stereoselectivity of [3+2] cycloaddition reactions

between N -methyl-phenylnitrone and trans -1-chloro-2-nitroethylene within the framework of molecular electron density theory, *New J. Chem.*, 2025, **49**(26), 11191–11202.

18 R. G. Parr and W. Yang, *Density-Functional Theory of Atoms and Molecules*, Oxford University Press, 1989.

19 P. Geerlings, F. De Proft and W. Langenaeker, Conceptual Density Functional Theory, *Chem. Rev.*, 2003, **103**, 1793–1874.

20 L. Domingo, M. Ríos-Gutiérrez and P. Pérez, Applications of the Conceptual Density Functional Theory Indices to Organic Chemistry Reactivity, *Molecules*, 2016, **21**, 748.

21 R. G. Parr, L. v. Szentpály and S. Liu, Electrophilicity Index, *J. Am. Chem. Soc.*, 1999, **121**, 1922–1924.

22 R. G. Parr and R. G. Pearson, Absolute hardness: companion parameter to absolute electronegativity, *J. Am. Chem. Soc.*, 1983, **105**, 7512–7516.

23 L. R. Domingo, E. Chamorro and P. Pérez, Understanding the Reactivity of Captodative Ethylenes in Polar Cycloaddition Reactions. A Theoretical Study, *J. Org. Chem.*, 2008, **73**, 4615–4624.

24 R. G. Parr and W. Yang, Density functional approach to the frontier-electron theory of chemical reactivity, *J. Am. Chem. Soc.*, 1984, **106**, 4049–4050.

25 W. Yang and W. J. Mortier, The use of global and local molecular parameters for the analysis of the gas-phase basicity of amines, *J. Am. Chem. Soc.*, 1986, **108**, 5708–5711.

26 R. F. W. Bader, Atoms in molecules, *Acc. Chem. Res.*, 1985, **18**, 9–15.

27 A. D. Becke, Density-functional thermochemistry. IV. A new dynamical correlation functional and implications for exact-exchange mixing, *J. Chem. Phys.*, 1996, **104**, 1040–1046.

28 L. R. Domingo, M. Ríos-Gutiérrez and P. Pérez, An MEDT study of the carbenoid-type [3 + 2] cycloaddition reactions of nitrile ylides with electron-deficient chiral oxazolidinones, *Org. Biomol. Chem.*, 2016, **14**, 10427–10436.

29 X. Krokidis, S. Noury and B. Silvi, Characterization of Elementary Chemical Processes by Catastrophe Theory, *J. Phys. Chem. A*, 1997, **101**, 7277–7282.

30 X. Krokidis, B. Silvi and M. Alikhani, Topological characterization of the isomerization mechanisms in XNO (X=H, Cl), *Chem. Phys. Lett.*, 1998, **292**, 35–45.

31 M. Chellegui, S. Benmetir, R. N. Salih, H. A. Mohammad-Salim, J. V. de Julián-Ortiz and A. Ben Ahmed, A molecular electron density theory investigation of the mechanism of intramolecular [3+2] cycloaddition (32CA) with the participation of nitrile N -oxide and ethene molecular segments, *New J. Chem.*, 2025, **49**(18), 7302–7313.

32 R. N. Salih, H. Mohammad-Salim and M. Algso, Mechanistic study of N-t-butyl nitrone and cyanoacetylene [3 + 2] cycloaddition: a combined DFT, docking, and ADMET approach, *Monatsh. Chem.*, 2025, **156**(4), 443–456.

33 L. R. Domingo, K. Kula and M. Ríos-Gutiérrez, Unveiling the Reactivity of Cyclic Azomethine Ylides in [3+2] Cycloaddition Reactions within the Molecular Electron Density Theory, *Eur. J. Org. Chem.*, 2020, **2020**, 5938–5948.

34 H. A. Mohammad-Salim, H. A. Basheer, H. H. Abdallah, A. Zeroual and L. A. Jamil, A molecular electron density theory study for [3+2] cycloaddition reactions of N -benzylcyclohexylnitrone with methyl-3-butenoate, *New J. Chem.*, 2021, **45**, 262–267.

35 L. R. Domingo, M. Ríos-Gutiérrez and N. Acharjee, A Molecular Electron Density Theory Study of the Chemoselectivity, Regioselectivity, and Diastereofacial Selectivity in the Synthesis of an Anticancer Spiroisoxazoline derived from α-Santonin, *Molecules*, 2019, **24**, 832.

36 S. A. Mohammed Salih, H. A. Basheer and H. A. Mohammad-Salim, Insights into the mechanism and stereoselectivity of the [3+2] cycloaddition reaction between N-methyl-C-(4-hydroxylphenyl) nitrone and maleic anhydride with a molecular electron density theory perspective, *Theor. Chem. Acc.*, 2022, **141**, 33.

37 L. R. Domingo and N. Acharjee, Unveiling the Chemo- and Regioselectivity of the [3+2] Cycloaddition Reaction between 4-Chlorobenzonitrile Oxide and β-Aminocinnamonitrile with a MEDT Perspective, *ChemistrySelect*, 2021, **6**, 4521–4532.

38 N. Acharjee, Unravelling the regio- and stereoselective synthesis of bicyclic N,O-nucleoside analogues within the molecular electron density theory perspective, *Struct. Chem.*, 2020, **31**, 2147–2160.

39 R. Huisgen, 1,3-Dipolar Cycloadditions. Past and Future, *Angew. Chem., Int. Ed. Engl.*, 1963, **2**, 565–598.

40 L. Domingo, Molecular Electron Density Theory: A Modern View of Reactivity in Organic Chemistry, *Molecules*, 2016, **21**, 1319.

41 R. M. Al-Mokhtar, H. Mohammad-Salim and M. Algso, Mechanistic study of nitrone and maleimide [3 + 2] cycloaddition: a combined DFT, BET study, docking, and ADMET approach from the MEDT perspective, *Struct. Chem.*, 2025, DOI: **10.1007/s11224-025-02455-0**.

42 B. Chakraborty, Solvent-free synthesis and 1,3-dipolar cycloaddition reactions of N - methyl-C-(2-furyl) nitrone in a ball mill and anticancer activities of the new cycloadducts, *J. Heterocycl. Chem.*, 2020, **57**, 477–485.

43 Y. Zhao and D. G. Truhlar, The M06 suite of density functionals for main group thermochemistry, thermochemical kinetics, noncovalent interactions, excited states, and transition elements: two new functionals and systematic testing of four M06-class functionals and 12 other function, *Theor. Chem. Acc.*, 2008, **120**, 215–241.

44 H. Mohammad-Salim, J. V. de Julián-Ortiz, K. A. Dahlous, M. S. Islam, T. M. Almutairi and S. Benmetir, Elucidating the mechanism and selectivity of [3 + 2] cycloaddition: a DFT and molecular docking investigation of the reaction of 6-butoxy-5,6-dihydro-4H-1,2-oxazine 2-oxide with dimethyl maleate, *Struct. Chem.*, 2025, **36**, 339–350.

45 A. Ouled Aitouna, H. Mohammad-Salim, A. Zeroual, A. Syed, A. H. Bahkali and J. V. de Julián-Ortiz, Investigation of the molecular mechanism and diastereoselectivity in the [3 + 2] cycloaddition reaction between acetonitrile oxide and Cis-3,4-Dichlorocyclobutene: Insights from MEDT and docking study, *Comput. Theor. Chem.*, 2023, **1228**, 114283.

46 S. Grimme, Density functional theory with London dispersion corrections, *Wiley Interdiscip. Rev.: Comput. Mol. Sci.*, 2011, **1**, 211–228.
47 K. Fukui, The path of chemical reactions - the IRC approach, *Acc. Chem. Res.*, 1981, **14**, 363–368.
48 M. J. Frisch, G. W. Trucks, H. B. Schlegel, G. E. Scuseria, M. A. Robb, J. R. Cheeseman, G. Scalmani, V. Barone, G. A. Petersson, H. Nakatsuji, X. Li, M. Caricato, A. V. Marenich, J. Bloino, B. G. Janesko, R. Gomperts, B. Mennucci, H. P. Hratchian, *Gaussian, 16, Revision B.01*, 2016, **https://gaussian.com/gaussian16/**.
49 L. R. Domingo, A new C–C bond formation model based on the quantum chemical topology of electron density, *RSC Adv.*, 2014, **4**, 32415–32428.
50 A. E. Reed, L. A. Curtiss and F. Weinhold, Intermolecular interactions from a natural bond orbital, donor-acceptor viewpoint, *Chem. Rev.*, 1988, **88**, 899–926.
51 E. R. Johnson, S. Keinan, P. Mori-Sánchez, J. Contreras-García, A. J. Cohen and W. Yang, Revealing Noncovalent Interactions, *J. Am. Chem. Soc.*, 2010, **132**, 6498–6506.
52 J. Contreras-García, E. R. Johnson, S. Keinan, R. Chaudret, J.-P. Piquemal, D. N. Beratan and W. Yang, NCIPLOT: A Program for Plotting Noncovalent Interaction Regions, *J. Chem. Theory Comput.*, 2011, **7**, 625–632.
53 T. Lu and F. Chen, Multiwfn: A multifunctional wavefunction analyzer, *J. Comput. Chem.*, 2012, **33**, 580–592.
54 S. Noury, X. Krokidis, F. Fuster and B. Silvi, Computational tools for the electron localization function topological analysis, *Comput. Chem.*, 1999, **23**, 597–604.
55 V. Liegeois, *DrawMol*, 2018, **https://www.unamur.be/drawmol**.
56 V. Liégeois, *DrawProfile*, 2024, **https://www.unamur.be/fr/sciences/chimie/recherche/ucpts/lct/drawsuite/drawprofile**.
57 *Flare™ for Ligand and Structure-Based Drug Design*, 2025, **https://cresset-group.com/software/flare/**.
58 Way2Drug, 2024, **https://www.way2drug.com/PASSOnline/**.
59 S. A. M. Salih, H. A. Basheer, J. V. de Julián-Ortiz and H. A. Mohammad-Salim, Unveiling the Stereoselectivity and Regioselectivity of the [3+2] Cycloaddition Reaction between N-methyl-C-4-methylphenyl-nitrone and 2-Propynamide from a MEDT Perspective, *Int. J. Mol. Sci.*, 2023, **24**, 9102.
60 M. D. Mellaoui, N. Acharjee, A. Imjjad, J. Koubachi, A. El Hammadi, H. Bourzi, S. El Issami, H. Zejli, M. Hochlaf and K. Abbiche, Unveiling the mechanism, selectivity, solvent and temperature effects on the [3 + 2] cycloaddition reaction of N-methyl-C-(2-furyl) nitrone with maleimide derivatives from the molecular electron density theory perspective, *Theor. Chem. Acc.*, 2023, **142**, 33.
61 M. Chellegui, B. Champagne and M. Trabelsi, Lewis acid-catalyzed Diels–Alder cycloaddition of 2,5-dimethylfuran and ethylene: a density functional theory investigation, *Theor. Chem. Acc.*, 2022, **141**, 21.
62 M. Chellegui, M. Trabelsi, B. Champagne and V. Liégeois, DFT Investigation of the Stereoselectivity of the Lewis-Acid-Catalyzed Diels–Alder Reaction between 2,5-Dimethylfuran and Acrolein, *ACS Omega*, 2025, **10**, 833–847.
63 M. Chellegui, S. Koudjina, I. Salhi, S. Benmetir, R. N. Salih, H. A. Mohammad-Salim, G. Y. S. Atohoun and J. V. de Julián-Ortiz, Mechanism and stereoselectivity of a [3 + 2] cycloaddition involving a glucosyl nitrone: a MEDT study, *Org. Biomol. Chem.*, 2025, **23**(20), 5016–5032.
64 M. Chellegui, A. I. Adjieufack, M. Trabelsi, V. Liégeois and B. Champagne, Unveiling the Reaction Mechanism of Diels-Alder Cycloadditions between 2,5-Dimethylfuran and Ethylene Derivatives Using Topological Tools, *ChemPhysChem*, 2025, **26**(6), 1–13.
65 L. R. Domingo, M. Ríos-Gutiérrez and P. Pérez, A molecular electron density theory study of the participation of tetrazines in aza-Diels–Alder reactions, *RSC Adv.*, 2020, **10**, 15394–15405.
66 P. Jaramillo, L. R. Domingo, E. Chamorro and P. Pérez, A further exploration of a nucleophilicity index based on the gas-phase ionization potentials, *J. Mol. Struct.:THEOCHEM*, 2008, **865**, 68–72.
67 M. J. Aurell, L. R. Domingo, P. Pérez and R. Contreras, A theoretical study on the regioselectivity of 1,3-dipolar cycloadditions using DFT-based reactivity indexes, *Tetrahedron*, 2004, **60**, 11503–11509.
68 L. R. Domingo, P. Pérez and J. A. Sáez, Understanding the local reactivity in polar organic reactions through electrophilic and nucleophilic Parr functions, *RSC Adv*, 2013, **3**(5), 1486–1494.
69 T. Weiser, AMPA Receptor Antagonists with Additional Mechanisms of Action: New Opportunities for Neuroprotective Drugs?, *Curr. Pharm. Des.*, 2002, **8**, 941–951.
70 G. Latacz, K. Sałat, A. Furgała-Wojas, A. Martyniak, A. Olejarz-Maciej, E. Honkisz-Orzechowska and E. Szymańska, Phenylalanine-Based AMPA Receptor Antagonist as the Anticonvulsant Agent with Neuroprotective Activity—In Vitro and In Vivo Studies, *Molecules*, 2022, **27**, 875.
71 A. L. Baggish and D. R. Hill, Antiparasitic Agent Atovaquone, *Antimicrob. Agents Chemother.*, 2002, **46**, 1163–1173.
72 L. R. Domingo and M. Ríos-Gutiérrez, A Useful Classification of Organic Reactions Based on the Flux of the Electron Density, *Sci. Radices*, 2023, **2**, 1–24.
73 C. A. Lipinski, F. Lombardo, B. W. Dominy and P. J. Feeney, Experimental and computational approaches to estimate solubility and permeability in drug discovery and development settings, *Adv. Drug Delivery Rev.*, 2001, **46**, 3–26.
74 A. K. Ghose, V. N. Viswanadhan and J. J. Wendoloski, A Knowledge-Based Approach in Designing Combinatorial or Medicinal Chemistry Libraries for Drug Discovery. 1. A Qualitative and Quantitative Characterization of Known Drug Databases, *J. Comb. Chem.*, 1999, **1**, 55–68.
75 D. F. Veber, S. R. Johnson, H.-Y. Cheng, B. R. Smith, K. W. Ward and K. D. Kopple, Molecular Properties That Influence the Oral Bioavailability of Drug Candidates, *J. Med. Chem.*, 2002, **45**, 2615–2623.
76 W. J. Egan, K. M. Merz and J. J. Baldwin, Prediction of Drug Absorption Using Multivariate Statistics, *J. Med. Chem.*, 2000, **43**, 3867–3877.

77 I. Muegge, S. L. Heald and D. Brittelli, Simple Selection Criteria for Drug-like Chemical Matter, *J. Med. Chem.*, 2001, **44**, 1841–1846.
78 M. Sadowski and K. Kula, Unexpected Course of Reaction Between (1E,3E)-1,4-Dinitro-1,3-butadiene and N-Methyl Azomethine Ylide—A Comprehensive Experimental and Quantum-Chemical Study, *Molecules*, 2024, **29**, 5066.
79 M. Sadowski, B. Synkiewicz-Musialska and K. Kula, (1E,3E)-1,4-Dinitro-1,3-butadiene—Synthesis, Spectral Characteristics and Computational Study Based on MEDT, ADME and PASS Simulation, *Molecules*, 2024, **29**, 542.
80 A. Klos, A. J. Tenner, K.-O. Johswich, R. R. Ager, E. S. Reis and J. Köhl, The role of the anaphylatoxins in health and disease, *Mol. Immunol.*, 2009, **46**, 2753–2766.
81 Y. Han, P. Wu, Z. Wang, Z. Zhang, S. Sun, J. Liu, S. Gong, P. Gao, T. Iwakuma, M. A. Molina-Vila, B. P.-C. Chen, Y. Zhang, T. Ji, Q. Mo, P. Chen, J. Hu, S. Wang, J. Zhou, H. Lu and Q. Gao, Ubiquinol-cytochrome C reductase core protein II promotes tumorigenesis by facilitating p53 degradation, *EBioMedicine*, 2019, **40**, 92–105.
82 M. A. Chiacchio, S. V. Giofrè, R. Romeo, G. Romeo and U. Chiacchio, Isoxazolidines as Biologically Active Compounds, *Curr. Org. Synth.*, 2016, **13**, 726–749.
83 M. Łysakowska, I. E. Głowacka, E. Honkisz-Orzechowska, J. Handzlik and D. G. Piotrowska, New 3-(Dibenzyloxyphosphoryl)isoxazolidine Conjugates of N1-Benzylated Quinazoline-2,4-diones as Potential Cytotoxic Agents against Cancer Cell Lines, *Molecules*, 2024, **29**, 3050.
84 W. A. Eneama, H. H. Salman and M. N. Mousa, Isoxazolidine Derivatives Exhibit Selective Antitumor Activity Against Breast Cancer Cells, *Academia Open*, 2024, **9**(2), DOI: **10.21070/acopen.9.2024.8148**.